Continuous-wave infrared optical gain and amplified spontaneous emission at ultralow threshold by colloidal HgTe quantum dots

Pieter Geiregat[1,2,3★], Arjan J. Houtepen[1,4], Laxmi Kishore Sagar[1,3], Ivan Infante[5], Felipe Zapata[5], Valeriia Grigel[1,3], Guy Allan[6], Christophe Delerue[6], Dries Van Thourhout[2,3] and Zeger Hens[1,3]

Colloidal quantum dots (QDs) raise more and more interest as solution-processable and tunable optical gain materials. However, especially for infrared active QDs, optical gain remains inefficient. Since stimulated emission involves multifold degenerate band-edge states, population inversion can be attained only at high pump power and must compete with efficient multi-exciton recombination. Here, we show that mercury telluride (HgTe) QDs exhibit size-tunable stimulated emission throughout the near-infrared telecom window at thresholds unmatched by any QD studied before. We attribute this unique behaviour to surface-localized states in the bandgap that turn HgTe QDs into 4-level systems. The resulting long-lived population inversion induces amplified spontaneous emission under continuous-wave optical pumping at power levels compatible with solar irradiation and direct current electrical pumping. These results introduce an alternative approach for low-threshold QD-based gain media based on intentional trap states that paves the way for solution-processed infrared QD lasers and amplifiers.

Colloidal quantum dots (QDs) combine size-tuneable electronic energy levels with a suitability for solution-based processing, priming them for numerous optoelectronic applications[1,2]. QD photodetectors[3], spectrometers[4], solar cells[5], white light-emitting diodes (LEDs) and displays[6] rely on the broad QD absorption spectrum with its size-dependent onset corresponding to the lowest energy exciton (X) transition and/or the tunable, narrow emission spectrum resulting from exciton recombination. Application development is further driven by unique characteristics such as multi-X generation[7] or room-temperature single-photon emission[8] and the possibility to fine-tune optoelectronic properties by heterostructure formation[9], doping[10] or alloying[11].

Tunable, low-cost and solution-processable gain media can equally impact on devices such as lasers or amplifiers[12]. Telecom applications operating at wavelengths around 1.3 or 1.55 μm, for example, make use of expensive epitaxially grown III–V lasers. Integrated photonics platforms based on silicon or silicon nitride, whereby small footprint photonic integrated circuits for data-communication, signal processing and sensing are fabricated using CMOS-compatible processes[13,14] even lack a native gain medium. In the case of silicon photonics, solutions relying on III–V die bonding, direct III–V epitaxy on silicon[15,16], erbium doping[17,18] or strained Ge[19] are heavily investigated but suffer from issues with cost, upscaling, efficiency or limited gain bandwidth. A solution-processable gain medium based on colloidal QDs can solve such issues, as recently demonstrated for silicon nitride photonics[20].

Stimulated emission involving the bandgap transition of QDs has been amply demonstrated[21–24]. Their use as gain media, however, remains limited since stimulated emission and absorption involve transitions between the same discrete band-edge states[12,25]. Since these are degenerate, QDs must contain more than one exciton (X) on average to achieve population inversion[21]. Next to this intrinsic drawback of two-level gain media, multi-X rapidly recombine through non-radiative Auger processes[26]. The population-inversion lifetime is therefore limited to a few tens of picoseconds, which means that gain thresholds are often reached only by femtosecond pulsed lasers[27]. Strategies to circumvent the limitations of multi-X gain involve slowing down Auger recombination through interfacial alloying in core/shell QDs and/or using large volume QDs,[28] strain[29] or two-dimensional platelets[25]. Alternatively, single-X gain has been demonstrated using so-called type II core/shell QDs[22], where repulsive X–X interactions lift the effective level degeneracy. Unfortunately, both approaches are restricted to a few materials—typically involving Cd-based QDs emitting in the visible—and gain thresholds remain incompatible with, for example, direct-current electrical pumping[25].

Here, we report on optical gain in dispersions of mercury telluride (HgTe) QDs and amplified spontaneous emission in HgTe QD polymer composites with average excitation densities $\langle N \rangle$ as low as 0.005 per QD, meaning that optical gain is attained by exciting only 1 out of 200 QDs in an ensemble. Intrinsic gain coefficients of 100–500 cm^{-1} are demonstrated and no decay of the population inversion is seen within the first nanoseconds after photoexcitation. We attribute this almost thresholdless gain to stimulated emission between the lowest conduction-band level and a shallow, empty state in the bandgap. The ensuing 4-level system results in high gain thresholds under continuous-wave (CW) optical pumping that now meet the requirements for direct current (DC) electrical pumping[30].

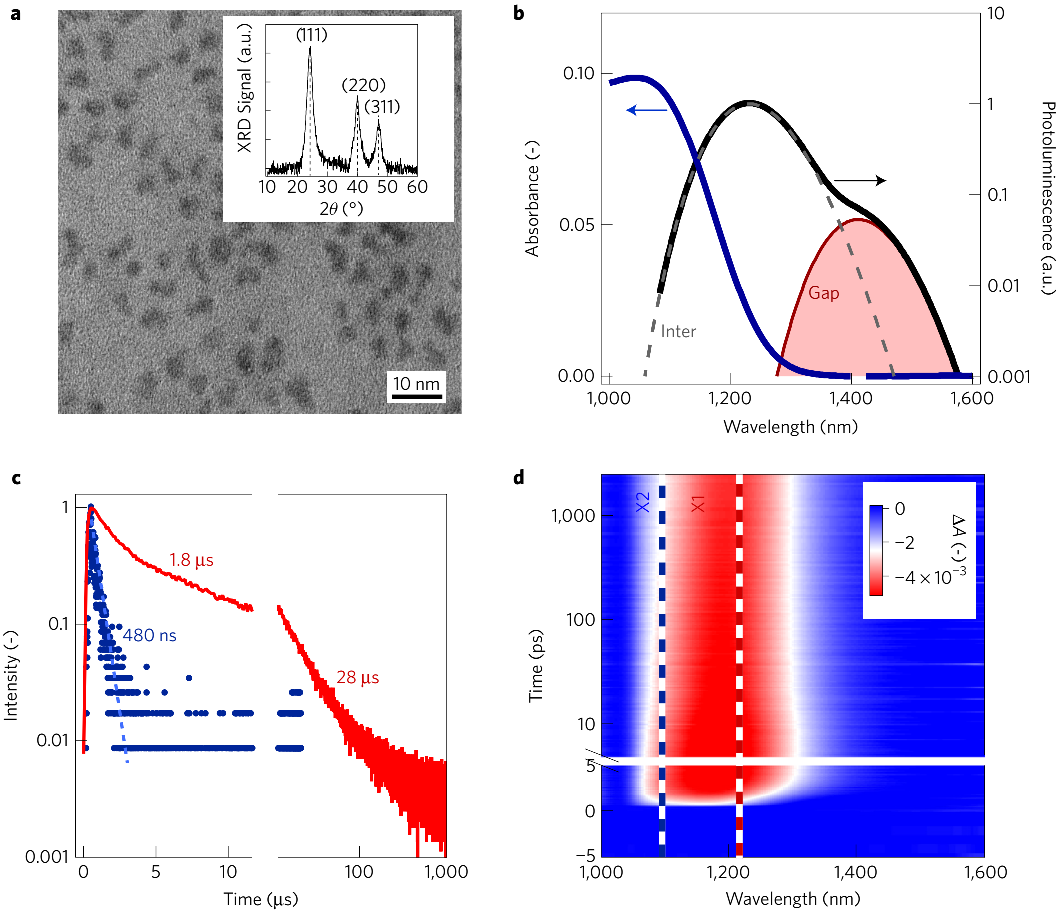

Figure 1 | Structural and linear optical properties of HgTe quantum dots (QDs). a, Transmission electron microscopy (TEM) image of 3.5 ± 0.3 nm dodecanethiol capped HgTe QDs. Inset shows the X-ray diffraction (XRD) pattern. **b**, Absorbance (blue) and emission (black) of HgTe QDs suspended in TCE as used in the transient absorption experiments. A clear additional emission band at lower energy is resolved (red) strongly red-shifted from the regular interband photoluminescence (black). These bands are already labelled as interband and gap emission, see further. **c**, Photoluminescence lifetime after excitation with 9 ns pulses at 532 nm for emission at the band edge (1.1 eV, blue) or in the low-energy band (0.85 eV, red). The average lifetime (see Methods) is determined to be 480 ns for the band-edge component and 1.8 to 28 μs for the emission band at lower energy. **d**, Two-dimensional transient absorption (ΔA) map as a function of wavelength and time, showing the broad bleach feature ($\Delta A < 0$) obtained after 700 nm photoexcitation at $t = 0$ with average number of absorbed photons per nanocrystal $\langle N \rangle = 0.1$. The band-edge features X_1 and X_2 as predicted by tight-binding calculations (see Supplementary Section 2) are added for comparison.

Basic properties of HgTe quantum dots

HgTe is a semi-metal with a direct negative bulk bandgap. Size quantization enables the bandgap of HgTe QDs to be tuned from the long-wave infrared down to the near-infrared, reaching approximately 1 eV for 3–4 nm QDs[31]. The colloidal HgTe QDs used here have been synthesized according to a modified literature procedure[32,33] (see Methods) leading to QDs with the zinc-blende crystal structure (see Fig. 1a). Their absorption spectrum exhibits a clear first exciton transition with a size-tunable maximum attained at approximately 1,100 nm for the example shown in Fig. 1b. The QD photoluminescence spectrum, on the other hand, is composed of a high intensity band peaking at approximately 1,225 nm, which we attribute to band-edge recombination and a low-intensity, sub-bandgap feature red-shifted by 100–150 meV relative to the band-edge emission. This combination of two emission bands is more pronounced at low temperature (see Supplementary Section 1). Importantly, while the band-edge emission has a luminescent lifetime of approximately 400 ns, the sub-bandgap transition shows a strongly delayed, multi-exponential emission that only drops to 1% of the original intensity after 100 μs (see Fig. 1c).

According to tight-binding calculations (see Supplementary Section 2)[34,35], the band-edge absorption of HgTe QDs consists of two exciton transitions, labelled X_1 and X_2, between the lowest conduction-band level (CB_1) and the two uppermost valence-band levels (VB_1, VB_2). Photoexcitation with a 700 nm pump pulse that creates on average $\langle N \rangle = 0.1$ excitons per QD yields a transient absorption (TA) spectrum that shows the reduction of the band-edge absorption due to state filling at around 1,200 nm (see Fig. 1d). This band-edge bleach narrows down and loses intensity in the first nanoseconds after pumping. By comparing the difference between spectral cuts at 5 ps, when carrier cooling is complete, and 2.5 ns, it follows that especially the bleach at the blue side of the first exciton transition is reduced (see Supplementary Section 3). In view of the tight-binding calculations, we attribute this change to the depletion of the higher-energy, higher-oscillator-strength X_2 manifold in favour of the lower-energy, lower-oscillator-strength X_1. The X_2–X_1 relaxation happens on a 700 ps timescale, a decay component also found in the time-resolved photoluminescence traces (see Supplementary Section 3). We thus conclude that the slow dynamics of the first exciton bleach reflect hole relaxation between the VB_2 and VB_1 states.

Nearly thresholdless gain

A most striking observation is the long-wavelength extension of the transient absorption bleach, covering the wavelength range of the sub-bandgap emission. This is better appreciated by looking

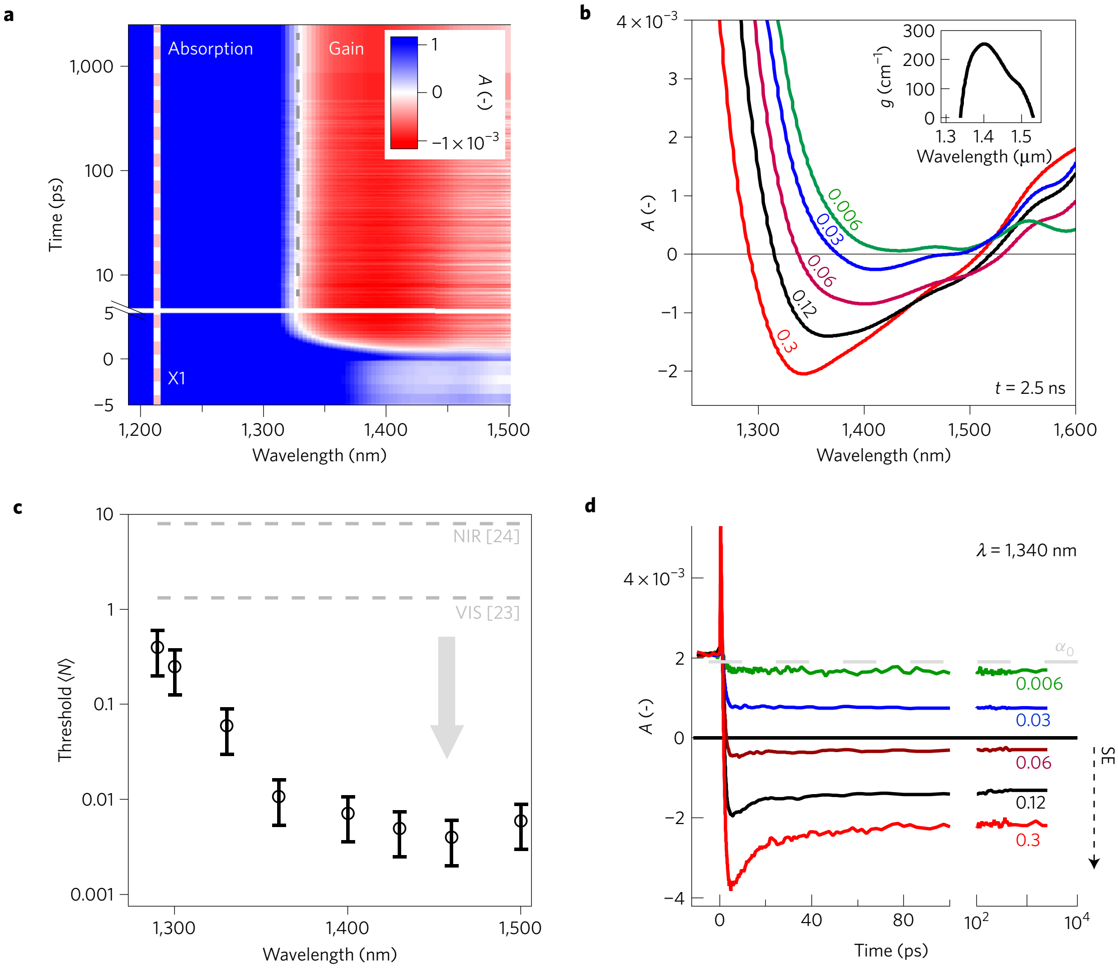

Figure 2 | Ultrafast spectroscopy. a, Nonlinear absorption A after photoexcitation at 700 nm, creating $\langle N\rangle = 0.06$. The grey dashed vertical line indicates transparency ($A = 0$), clearly separating a region of (blue) absorption and (red) amplification. X1 denotes the lowest interband exciton (see also Fig. 1d). **b**, A spectra, taken 2.5 ns after photoexcitation for different pump fluences. Inset shows the intrinsic material gain obtained from rescaling the A spectra (see Methods and text). **c**, Wavelength-dependent gain threshold as obtained from Fig. 3b. The dashed horizontal lines indicate the lowest thresholds reported in literature for visible (VIS)[23] and near-infrared (NIR)[24] emitting QDs. **d**, Time dependence of A at 1,340 nm for increasing fluence. We observe a crossover to net stimulated emission (SE) at $\langle N\rangle = 0.06$ and an absence of dynamics within the measured time window.

at the nonlinear absorbance $A = \Delta A + A_0$, where Fig. 2a provides an example recorded for a $\langle N\rangle = 0.06$ excitation density. Here, the vertical dashed grey line delineates regions of net absorbance ($A > 0$, blue) and amplification ($A < 0$, red). Figure 2b displays spectral cuts of nonlinear absorption maps at a 2.5 ns delay obtained with different pump fluences. Note that this delay strongly exceeds the multi-X lifetime, such that QDs contain at most a single exciton. At very low excitation density ($\langle N\rangle < 0.006$) absorption dominates and A is positive at all wavelengths. With increasing fluence, A turns negative at wavelengths far to the red of the X_1 band-edge transition. Significant amplification is observed for $\langle N\rangle > 0.03$—a most remarkable observation as this is well below the usual $\langle N\rangle = 1$ threshold density for optical gain in a regular 2-level system. At higher fluences, yet well below $\langle N\rangle = 1$ excitation densities, this gain region extends from 1,300 to 1,500 nm, a range covering the technologically relevant transparency windows of commercial glass fibre. Larger HgTe QDs exhibit a similar gain band at longer wavelengths (see Supplementary Section 4).

Figure 2c shows more explicitly that HgTe QDs reach transparency, as derived from TA spectra, at thresholds $\langle N\rangle$ dropping to 0.005 beyond 1,450 nm. Such a threshold is two to three orders of magnitude lower than the best results reported for visible[23,25] and near-infrared[24] QDs, respectively (dashed horizontal lines in Fig. 2c), which typically rely on stimulated emission by bi- or multi-excitons. As can be seen in Fig. 2a, optical gain is attained almost instantaneously after femtosecond pumping above the threshold intensity, especially at longer wavelengths. Moreover, focusing on nonlinear absorption traces at $\lambda = 1{,}340$ nm, Fig. 2d attests that gain persists throughout the entire accessible time window, with no indication of multi-exciton decay for an $\langle N\rangle = 0.06$ initial exciton density. At higher exciton densities, multi-exciton Auger recombination shows up with an approximately 50 ps lifetime, yet also then, gain does not disappear as multi-excitons recombine (see Fig. 2d and Supplementary Section 5).

In the inset of Fig. 2b, we have rescaled the nonlinear absorbance to a nonlinear absorption or gain coefficient using the expression[36]:

$$g_i(\lambda) = -\frac{\mu_i(400)}{A_0(400)} A(\lambda) \qquad (1)$$

Here, $\mu_i(400)$ is the intrinsic absorption coefficient of HgTe QDs at 400 nm—which we calculate using bulk optical constants (see Supplementary Section 6). By definition, $g_i(\lambda)$ yields the gain coefficient of a fictitious material in which the QDs occupy 100% of the volume, a quantity that can be called the material gain. As shown by the inset of Fig. 2b, the intrinsic material gain easily reaches 250 cm^{-1} when $\langle N\rangle = 0.06$ in a wavelength range tunable by the QD size (see Supplementary Section 5). Such a material gain is in between

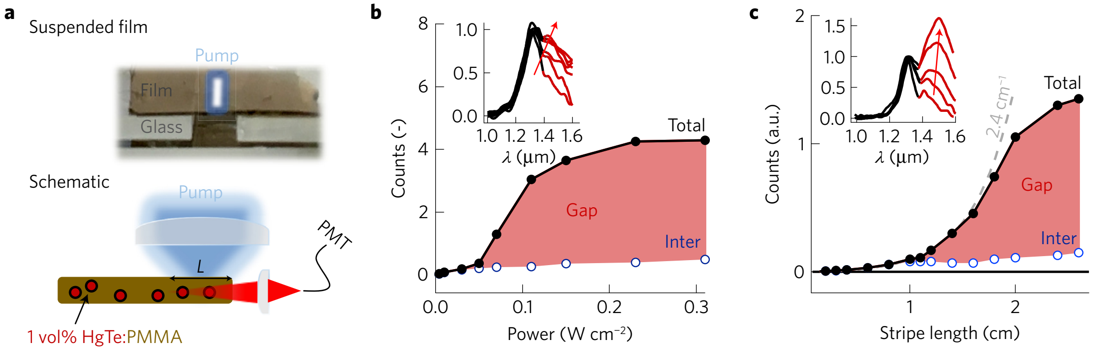

Figure 3 | Optical gain in hybrid PMMA-1%HgTe nanocomposites under continuous-wave (CW) excitation at 447 nm. a–c, Free-standing thin films are used for studying amplified spontaneous emission with a stripe excitation profile (**a**), both for increasing pump power (**b**) and stripe length *L* (**c**). Supralinear increase of the light emitted at the long-wavelength side of the spectrum (indicated in red on normalized spectra in insets) is clearly observed, both for increasing pump power and stripe length. We note that both the total light intensity and the decomposed gap contribution show this behaviour. A threshold of 40 mW cm^{-2} is determined and, from the stripe-length-dependent measurements, a net modal gain coefficient of 2.4 cm^{-1} is extracted (for an excitation level of 100 mW cm^{-2}).

the gain obtained in commonly used erbium-doped fibre amplifiers (EDFA) (10^{-2}–10^{-3} cm^{-1}) and that of epitaxially grown III–V semiconductors (∼10^3 cm^{-1})[37,38] and colloidal QDs (∼10^3 cm^{-1})[39].

Amplified spontaneous emission in nanocomposites

The gain coefficients and the lifetime of the population inversion should suffice for stimulated emission to amplify spontaneous emission (ASE) in thin films of HgTe QDs[21]. To verify this idea, we prepared nanocomposite films of HgTe QDs dispersed in polymethyl methacrylate (PMMA) at QD volume fractions of 0.1% and 1% (see Fig. 3a and Methods). In full agreement with HgTe QDs dispersed in C_2Cl_4, TA maps of PMMA/HgTe films attest net amplification at the long-wavelength side of the band-edge transition and their PL spectrum features two emission bands, with the high-energy band corresponding to the band-edge emission (see Supplementary Section 7). As further shown in Supplementary Section 7, pumping 1% PMMA/HgTe films with 110 fs amplified pulses at 400 nm results in a marked enhancement of the long-wavelength emission band with increasing fluence. In addition, a clear supralinear increase of the total light intensity beyond 6 μJ cm^{-2} is observed, which can be evaluated even further by decomposing the emission spectrum into an interband and a 'gap-state' component. Most remarkably, a similar behaviour is observed under CW pumping using a 447 nm laser diode (see Fig. 3b and Methods). Under such conditions, amplification of the gap-state emission is observed when pump powers exceed approximately 40 mW cm^{-2}. In stark contrast with the behaviour of 1% PMMA/HgTe nanocomposites, the emission spectrum of 0.1% nanocomposites is independent of the pump power (see Supplementary Section 7). Hence, the amplification of the gap-state emission in 1% nanocomposites is not a spurious photo-induced effect caused by, for example, QD charging.

We analysed the amplification of the gap-state emission more quantitatively by variable stripe length (VSL) measurements using a set-up outlined in Fig. 3a. Using femtosecond pumping at a fixed fluence of 10 μJ cm^{-2}, we observe a supralinear increase of the total light output with increasing excitation stripe length (see Supplementary Section 7). The variation of the spectra as a function of stripe length already indicates that this reflects the amplification of the gap-state emission, a conclusion that is confirmed by plotting the gap-state emission intensity as a function of stripe length. Again, these characteristics are even more prominent in VSL measurements under CW pumping. As shown in Fig. 3c, the total light output shows a pronounced supralinear increase that concurs with an intensifying and narrowing gap-state emission—two clear signatures of ASE. From the exponential increase of the gap-state emission intensity, we obtain a CW gain coefficient of 2.4 cm^{-1} under the given pump conditions. As shown in Supplementary Section 8, this result is consistent with the CW pump power used and the optical characteristics derived from photoluminescence and transient absorption spectroscopy. This observation constitutes the first demonstration of CW pumped ASE by colloidal zero-dimensional QDs and it shows that CW gain by colloidal semiconductors is possible at extremely low pump thresholds, thanks to a combination of low-threshold excitation density and a long population-inversion lifetime. The threshold fluence of 40 mW cm^{-2} found here can be directly compared to the approximately 5,000 mW cm^{-2} threshold reported for CW ASE in films of two-dimensional CdSe nanoplatelets—the lowest threshold reported to date[25,29].

HgTe QDs as 4-level systems

HgTe QDs exhibit optical gain well below the one-exciton-per-QD limit, as evidenced by their low fluence threshold for gain and ASE and the long-lived population inversion. Moreover, especially at the long-wavelength edge of the gain window, the emitting transition involved has no counterpart in absorption at that specific wavelength. While such a condition can be achieved with so-called 4-level systems, it cannot be simply met by the QD bandgap transition. This results in the need for multi-exciton gain or, at best, thresholds above $\langle N \rangle = 2/3$ for core/shell QDs engineered to show single-exciton gain[22]. A further lowering of the gain threshold can result when stimulated emission is downshifted from the band-edge absorption by, for example, electron–phonon coupling[40]. Alternatively, almost thresholdless gain may result from emitting transitions of a band-edge carrier to a localized state in the QD bandgap that lack a counterpart in absorption. Although it is well known that localized bandgap states can be deliberately introduced in QDs by doping[41], or may result from incomplete surface passivation[42], optical gain via such states has never been reported.

As shown in Fig. 1b,c, HgTe QDs feature a dual-band emission where the longer wavelength, sub-bandgap emission overlaps with the observed optical gain window. This implies that the sub-bandgap stimulated emission in HgTe QDs cannot result from the band-edge emission being red-shifted by electron–phonon coupling, as this should lead to a single, red-shifted emission band. Sub-bandgap photoluminescence may, however, involve transitions of CB electrons to empty gap states or of VB holes to occupied gap states. The former is more likely in the present case (see below). As the same transition can give rise to stimulated emission, optical gain in HgTe QDs could be interpreted through a single-electron level scheme as shown in Fig. 4a, where optical gain is related to a transition of a CB electron to a shallow, empty state in the bandgap.

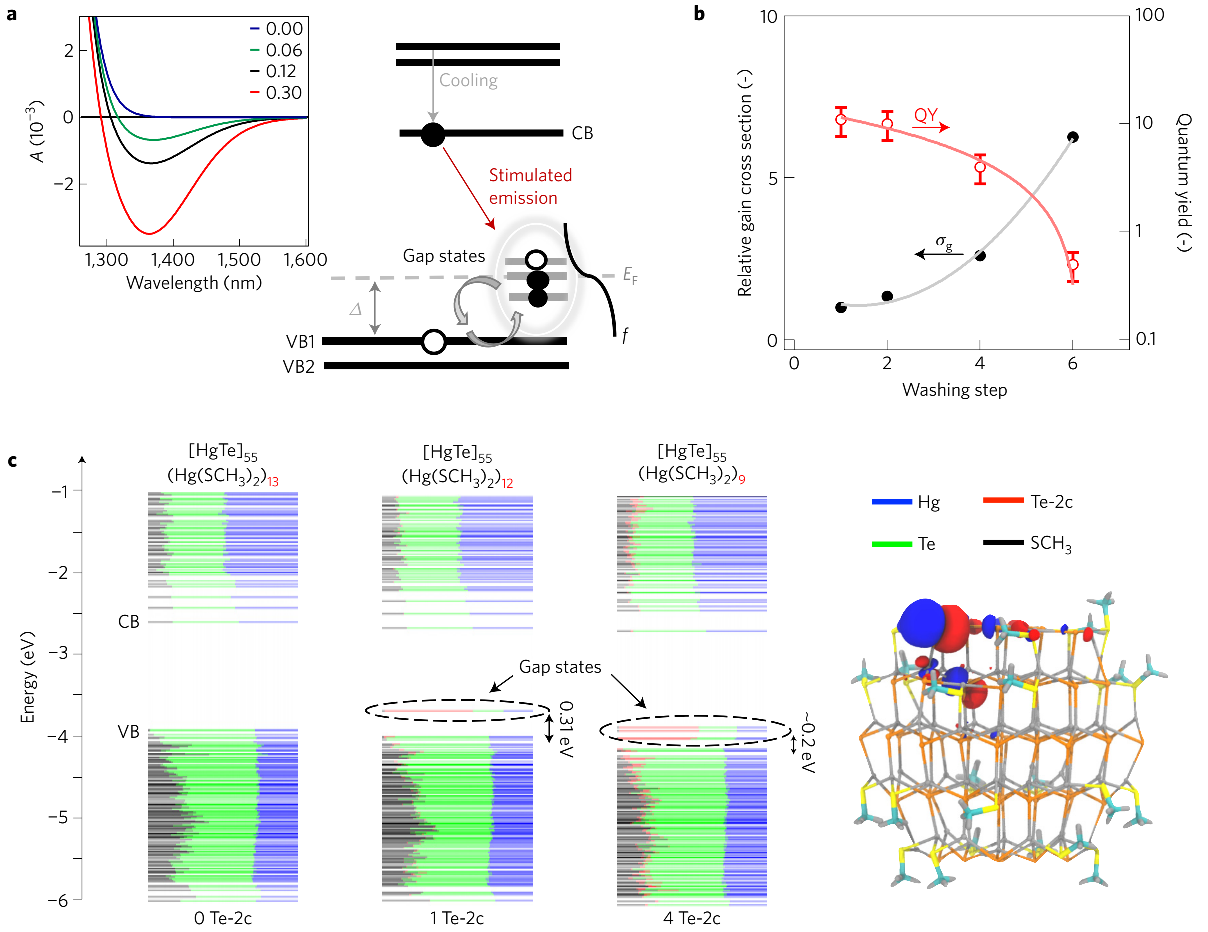

Figure 4 | HgTe gain model and surface chemistry. a, Proposed 4-level scheme where the stimulated emission involving a conduction-band (CB) electron to empty surface defect levels close to the valence band (VB1/2) has no counterpart in absorption, leading to a gain without threshold. (Inset) Absorbance for different exciton densities based on the proposed defect model (see main text). **b**, Increase of gain cross-section (at 1,340 nm, black solid markers) and concomitant decrease in photoluminescence quantum yield (QY; log scale, red empty markers) with subsequent washing steps. **c**, Energy level spectrum of (left) a $[HgTe]_{55}(Hg(SCH_3)_2)_{13}$ model nanocrystal, (centre) the same nanocrystal after removal of one $Hg(SCH_3)_2$ complex and (right) the same nanocrystal after removal of four $Hg(SCH_3)_2$ complexes, calculated using density functional theory. The colours measure the projection of each state on (blue) Hg atoms, (green) Te atoms, (black) methanethiolate and (red) di-coordinated Te on different atom/fragment types. Successive removal of one $Hg(SCH_3)_2$ complexes results in a band of gap states separated by about 100 meV from the highest occupied molecular orbital (HOMO). The inset shows the wavefunction of the gap state. It can be seen that this state largely corresponds to the 5*p* orbital of a two-coordinated tellurium surface atom that is orthogonal to neighbouring Hg 6*s* orbitals.

Writing the occupation of the gap state as f (that is, the Fermi–Dirac distribution) and the absorbance of the CB/gap-state transition as A_g, the ensemble averaged absorbance linked to gap-state transition reads within the proposed model:

$$\langle A\rangle = 2(1-\langle N\rangle)fA_g + \langle N\rangle fA_g - \langle N\rangle(1-f)A_g \qquad (2)$$

Here, we only consider absorption by unexcited QDs and absorption and stimulated emission by singly excited QDs, where $\langle N\rangle$ then coincides with the fraction of excited QDs. According to equation (2), transparency is attained when $\langle N\rangle = 2f$, indicating that low-threshold gain will develop in the low-energy tail of gap transition—where f tends to zero—and shift towards higher energies with increasing excitation densities. This also follows from a more detailed model calculation shown in Fig. 4a, which indeed reproduces the initial opening of the gain band at the red side of the gap-state emission with increasing excitation density, in line with the nonlinear absorbance spectra shown in Fig. 2b (see also Supplementary Section 8 for more details). In addition, the model predicts that the occupancy of the band-edge states will directly affect the optical gain. This relation explains why the transient gain appears almost instantaneously after optical pumping and, as the transient gain does not show the imprint of the slow, 700 ps VB_2/VB_1 cooling, it indicates that stimulated emission involves a CB/gap-state transition.

An apparent issue with the model introduced is the HgTe band-edge emission. Depending on the rapid capture or not of the photoexcited hole, it should be fully quenched or appear as a relaxation pathway in competition with the gap-state transition. However, an estimate of the hole-capture rate points towards a large spread in capture times, depending on the energy difference between the gap state and the valence-band edge (see Supplementary Section 9). Especially for larger energy differences, capture times may exceed the measured luminescence lifetime, suggesting that a fraction of the HgTe QDs can indeed show band-edge emission as hole capture is too slow, while for the majority of the QDs the band-edge transition is quenched by rapid hole capture. In such heterogeneous ensemble, the combined observation of band-edge emission and long-lifetime sub-bandgap (stimulated) emission is possible. Moreover, as already mentioned before, the long carrier lifetime linked to the gap-state emission can account for the low CW optical gain pumping thresholds as found here (see Fig. 1c and Supplementary Section 8).

Stimulated emission through surface traps

To further identify the origin of the gap state, we analysed the optical gain of a given batch of HgTe QDs after successive purification cycles (see Methods and Supplementary Section 9). As shown in Fig. 4c, increased washing leads to a drop in photoluminescence quantum yield and a concomitant supralinear increase of the gain cross-section of an ensemble of HgTe QDs. Nuclear magnetic resonance (NMR) spectroscopy and elemental analysis indicates that purification results in a joint loss of both Hg and surface ligands from the QDs, possibly as mercury thiolate complexes.

The removal of such Z-type ligands[43] is well known to introduce surface trap states in CdX $(X = S,Se,Te)$ QDs[44–46]. Following the approach of Houtepen *et al.*[46] (see Methods and Supplementary Section 10), we used density functional theory (DFT) to construct a $\sim$2.0 nm model of a zinc-blende HgTe QD capped with methane thiolate. Figure 4c shows the energy level spectrum of this HgTe model QD, where the colours measure the projection of each state on different atom/fragment types. Most importantly, upon removal of one to four Z-type $Hg(SCH_3)_2$ ligands from the surface, a manifold of mostly localized gap states develops at $\sim$0.1 eV above top of the valence band; in close agreement with the experimental observations. Similar to what was predicted for CdX, these states originate from the 5*p* lone pair of two-coordinated tellurium surface atoms. As shown in Supplementary Section 10, DFT predicts that the oscillator strength of the HgTe gap-state transition exceeds that of the corresponding transitions in CdTe and CdSe QDs by two orders of magnitude, which can be linked to the stronger delocalization of the two-coordinated Te surface state in HgTe. Hence, while surface states linked to two-coordinated surface chalcogenides may be ubiquitous in II–VI QDs, the balance between the oscillator strength of the gap-state transition and spurious photo-induced absorption seems key to attain optical gain.

In summary, HgTe QDs exhibit ultralow threshold optical gain and amplification of spontaneous emission, which we attribute to a transition between the conduction-band edge and an empty surface-localized gap state. This makes HgTe QDs a 4-level system, for which population inversion can be reached at pump fluences substantially below the one-exciton-per-QD level. The gain and ASE thresholds observed here are up to two orders of magnitude lower than in recent literature reports[22,23,25]. Especially the demonstration of continuous-wave ASE at a 40 mW cm^{-2} threshold stands out. Such thresholds match the power density of unconcentrated sunlight and correspond to an electrical DC density of approximately 20 mA cm^{-2}, a level attained in state-of-the-art DC-driven, electroluminescent QD-LEDs[30,47,48]. We thus conclude that the gain characteristics of HgTe QDs demonstrated here introduce an approach to QD-based gain materials that offers unique prospects of low CW lasing thresholds, spectral tuning and solution-processing.

Methods

Methods, including statements of data availability and any associated accession codes and references, are available in the online version of this paper.

Received 24 March 2017; accepted 1 September 2017;
published online 9 October 2017

References

1. Yin, Y. & Alivisatos, P. Colloidal nanocrystal synthesis and the organic-inorganic interface. *Nature* **437,** 664–670 (2005).
2. Kovalenko, M. V. *et al*. Prospects of nanoscience with nanocrystals. *ACS Nano* **9,** 1012–1057 (2015).
3. Keuleyan, S., Lhuillier, E., Brajuskovic, V. & Guyot-Sionnest, P. Mid-infrared HgTe colloidal quantum dot photodetectors. *Nat. Photon.* **5,** 489–493 (2011).
4. Bao, J. & Bawendi, M. G. A colloidal quantum dot spectrometer. *Nature* **523,** 67–70 (2015).
5. Wang, X. *et al*. Tandem colloidal quantum dot solar cells employing a graded recombination layer. *Nat. Photon.* **5,** 480–484 (2011).
6. Kim, T. *et al*. Full-colour quantum dot displays fabricated by transfer printing. *Nat. Photon.* **5,** 176–182 (2011).
7. Beard, M. C. *et al*. Comparing multiple exciton generation in quantum dots to impact ionization in bulk semiconductors: implications for enhancement of solar energy conversion. *Nano Lett.* **10,** 3019–3027 (2010).
8. Galland, C. *et al*. Two types of luminescence blinking revealed by spectroelectrochemistry of single quantum dots. *Nature* **479,** 203–207 (2011).
9. De Geyter, B. *et al*. The different nature of band edge absorption and emission in colloidal PbSe/CdSe core/shell quantum dots. *ACS Nano* **5,** 58–66 (2011).
10. Norris, D. J., Efros, A. L. & Erwin, S. C. Doped nanocrystals. *Science* **319,** 1776–1779 (2008).
11. Aubert, T. *et al*. Homogeneously alloyed CdSeS quantum dots: an efficient synthesis for full optical tunability. *Chem. Mater.* **25,** 2388–2390 (2013).
12. Nurmikko, A. What future for quantum dot-based light emitters? *Nat. Nanotech.* **10,** 1001–1004 (2015).
13. Jenkins, A. Silicon lasers: the final frontier. *Nat. Photon.* **1,** 240 (2007).
14. Simply silicon. *Nat. Photon.* **4,** 491 (2010).
15. Chen, R. *et al*. Nanolasers grown on silicon. *Nat. Photon.* **5,** 170–175 (2011).
16. Wang, Z. *et al*. Room temperature InP DFB laser array directly grown on (001) silicon. *Nat. Photon.* **9,** 837–842 (2015).
17. Franzo, G., Priolo, F., Coffa, S., Polman, A. & Carnera, A. Room-temperature electroluminescence from Er-doped crystalline Si. *Appl. Phys. Lett.* **64,** 2235–2237 (1994).
18. Daldosso, N. *et al*. Erbium and silicon nanocrystals for light amplification. *Conf. Proc.—Lasers and Electro-Optics Society Annual Meeting-LEOS* 933–934 (2007).
19. Geiger, R. *et al*. Analysis of enhanced light emission from highly strained germanium microbridges. *Nat. Photon.* **7,** 466–472 (2013).
20. Xie, W. *et al*. On-chip integrated quantum-dot silicon-nitride microdisk lasers. *Adv. Mater.* **29,** 1604866 (2017).
21. Klimov, V. I. *et al*. Optical gain and stimulated emission in nanocrystal quantum dots. *Science* **290,** 314–317 (2000).
22. Klimov, V. I. *et al*. Single-exciton optical gain in semiconductor nanocrystals. *Nature* **447,** 441–446 (2007).
23. Dang, C. *et al*. Red, green and blue lasing enabled by single-exciton gain in colloidal quantum dot films. *Nat. Nanotech.* **7,** 335–339 (2012).
24. Schaller, R. D., Petruska, M. a. & Klimov, V. I. Tunable near-infrared optical gain and amplified spontaneous emission using PbSe nanocrystals. *J. Phys. Chem. B* **107,** 13765–13768 (2003).
25. Grim, J. Q. *et al*. Continuous-wave biexciton lasing at room temperature using solution-processed quantum wells. *Nat. Nanotech.* **9,** 891–895 (2014).
26. Klimov, V. I. Quantization of multiparticle auger rates in semiconductor quantum dots. *Science* **287,** 1011–1013 (2000).
27. Chen, Y. *et al*. Flexible distributed-feedback colloidal quantum dot laser. *Appl. Phys. Lett.* **99,** 241103 (2011).
28. García-Santamaría, F. *et al*. Suppressed auger recombination in 'giant' nanocrystals boosts optical gain performance. *Nano Lett.* **9,** 3482–3488 (2009).
29. Fan, F. *et al*. Continuous-wave lasing in colloical quantum dot solids enabled by facet-selective epitaxy. *Nature* **544,** 75–79 (2017).
30. Caruge, J. M., Halpert, J. E., Wood, V., Bulović, V. & Bawendi, M. G. Colloidal quantum-dot light-emitting diodes with metal-oxide charge transport layers. *Nat. Photon.* **2,** 247–250 (2008).
31. Keuleyan, S., Kohler, J. & Guyot-Sionnest, P. Photoluminescence of mid-infrared HgTe colloidal quantum dots. *J. Phys. Chem. C* **118,** 2749–2753 (2014).
32. Keuleyan, S., Lhuillier, E. & Guyot-Sionnest, P. Synthesis of colloidal HgTe quantum dots for narrow mid-IR emission and detection. *J. Am. Chem. Soc.* **133,** 16422–16424 (2011).
33. Kim, S. *et al*. Bandgap engineered monodisperse and stable mercury telluride quantum dots and their application for near-infrared photodetection. *J. Mater. Chem.* **21,** 15232–15236 (2011).
34. Allan, G. & Delerue, C. Tight-binding calculations of the optical properties of HgTe nanocrystals. *Phys. Rev. B* **86,** 165437 (2012).
35. Keuleyan, S. E., Guyot-sionnest, P., Delerue, C. & Allan, G. Mercury telluride colloidal quantum dots: electronic structure, size-dependent spectra, and photocurrent detection up to 12 μm. *ACS Nano* **8,** 8676–8682 (2014).
36. Hens, Z. & Moreels, I. Light absorption by colloidal semiconductor quantum dots. *J. Mater. Chem.* **22,** 10406–10415 (2012).
37. Kittel, C. *Introduction to Solid State Physics* (John Wiley, 2005).
38. Jiang, S. B. *et al*. Er^{3+}-doped phosphate glasses for fiber amplifiers with high gain per unit length. *J. Non-Cryst. Solids* **263,** 364–368 (2000).
39. Pietryga, M. *et al*. Spectroscopic and device aspects of nanocrystal quantum dots. *Chem. Rev.* **116,** 10513–10622 (2016).
40. Geiregat, P., Allan, G., Hens, Z. & Delerue, C. Single-exciton optical gain in semiconductor nanocrystals: positive role of electron-phonon coupling. *Phys. Rev. B* **93,** 115416 (2016).

41. Viswanatha, R., Brovelli, S., Pandey, A., Crooker, S. & aKlimov, V. I. Copper-doped inverted core/shell nanocrystals with 'permanent' optically active holes. *Nano Lett.* **11,** 4753–4758 (2011).
42. Boehme, S. C. *et al*. Density of trap states and Auger-mediated electron trapping in CdTe quantum-dot solids. *Nano Lett.* **15,** 3056–3066 (2015).
43. De Roo, J., Van Driessche, I., Martins, J. C. & Hens, Z. Colloidal metal oxide nanocrystal catalysis by sustained chemically driven ligand displacement. *Nat. Mater.* **15,** 517–521 (2016).
44. Hassinen, A. *et al*. Short-chain alcohols strip X-type ligands and quench the luminescence of PbSe and CdSe quantum dots, acetonitrile does not. *J. Am. Chem. Soc.* **134,** 20705–20712 (2012).
45. Anderson, N. C., Hendricks, M. P., Choi, J. J. & Owen, J. S. Ligand exchange and the stoichiometry of metal chalcogenide nanocrystals: spectroscopic observation of facile metal-carboxylate displacement and binding. *J. Am. Chem. Soc.* **135,** 18536–18548 (2013).
46. Houtepen, A., Hens, Z., Owen, J. S. & Infante, I. On the origin of surface traps in colloidal II–VI semiconductor nanocrystals. *Chem. Mater.* **29,** 752–761 (2017).
47. Kim, T.-H. *et al*. Full-colour quantum dot displays fabricated by transfer printing. *Nat. Photon.* **5,** 176–182 (2011).
48. Kwak, J. *et al*. Bright and efficient full-color colloidal quantum dot light-emitting diodes using an inverted device structure. *Nano Lett.* **12,** 2362–2366 (2012).

Acknowledgements

This research is funded by Ghent University (Special Research Fund BOF), BelSPo (IAP 7.35, photonics@be), EU-FP7 (Navolchi), NWO (Vidi grant, No. 723.013.002) Horizon 2020 ITN Phonsi and ERC-ULPICC and ERC-PoC Interdot. P.G. acknowledges the FWO Vlaanderen for a postdoctoral fellowship. S. Flamee is acknowledged for TEM imaging of the QDs and R. Van Deun and P. Smet are acknowledged for the use of the steady-state and time-resolved photoluminescence set-up and the cryogenic spectroscopy, respectively.

Author contributions

P.G. carried out the steady-state and time-resolved photoluminescence, and the ultrafast experiments, analysed the data, aided in theory development and wrote the manuscript; A.J.H. supervised the experiments, aided in theory discussions and wrote the manuscript; I.I. and F.Z. performed the DFT calculations and wrote the manuscript; L.K.S. synthesized the HgTe QDs and performed structural characterization (TEM, XRD); C.D. and G.A. carried out the tight-binding simulations and aided in theory development; D.V.T. aided in theory discussions and supervised the research; Z.H. initiated and supervised the research, aided in the theory development and wrote the manuscript.

Additional information

Supplementary information is available in the online version of the paper. Reprints and permissions information is available online at www.nature.com/reprints. Publisher's note: Springer Nature remains neutral with regard to jurisdictional claims in published maps and institutional affiliations. Correspondence and requests for materials should be addressed to P.G.

Competing financial interests

The authors declare no competing financial interests.

Methods

Synthesis of HgTe quantum dots and composites. Colloidal HgTe QDs were synthesized by modifying the procedure of Keuleyan *et al.*[32] and Sungwoo and colleagues[33]. As such, 270 mg (1 mmol) of $HgCl_2$, 1.6 ml (6 mmol) of dodecanethiol (DDT) and 8 ml of oleylamine (OLA) were mixed in a 25 ml flask and degassed under vacuum at 100 °C for one hour, after which the reaction mixture was placed under nitrogen while keeping the temperature at 60 °C. Next, 1 ml of a 1 M solution of tellurium in *tri*-octylphosphine was rapidly injected and a black-coloured reaction mixture was obtained within a few seconds. The reaction mixture was kept at the injection temperature to allow for QD growth for 1 min (1,220 nm emission) to 3 min (1,300 nm emission), after which the reaction was quenched by injecting 10 ml of toluene and cooling with a water bath. As-obtained HgTe QDs were purified twice using toluene and methanol. PMMA or polymethyl methacrylate, was purchased from Sigma Aldrich with a molecular weight of 120,000 and a mass density of 1.19 g cm^{-3}. 0.96 g of PMMA was dissolved in 10 ml of toluene to obtain a 5 m% solution. From this stock solution, 1 ml was mixed with a given HgTe QD solution in toluene to obtain a volume fraction of QDs of 0.1 to 1% relative to PMMA. These composites were dropcast or spincoated on glass substrates to achieve different film thicknesses of a few hundreds of nanometres to several micrometres. We use PMMA composites since dropcasting or spincoating HgTe-only dispersions does not provide thick and optically smooth films. The composite approach also allows one to tune the volume fraction, which is useful to obtain a reference sample for the ASE experiments.

Linear optical properties. Lifetime measurements were carried out using a Hamamatsu near-infrared photomultipler tube in combination with a pulsed Nd:YAG laser operated at 532 nm. Excitation pulses were 9 ns at a repetition rate of 10 Hz. Samples were prepared by diluting a solution of QDs in dry tetrachloroethylene (Aldrich) to an optical density of 0.1 at the excitation wavelength of 650 nm. The average lifetime is defined as $\langle t\rangle = \left(\int tI(t)\mathrm{d}t\right) / \left(\int I(t)\right)$. The quantum yield is determined using an integrating sphere method which requires no standard dye, thus resolving a common issue for near-infrared emitters.

Tight-binding calculations. The electronic structure and the optical properties of the HgTe QDs have been studied theoretically following closely the methodology described by Delerue and colleagues[34]. Details can be found in Supplementary Section 2.

DFT modelling. A non-stoichiometric $[\text{HgTe}]_{55}(\text{Hg(SCH}_3)_2)_{13}$ QD of about 2.0 nm in diameter was prepared from the bulk zinc-blende crystal. The electronic structure and density of states of the pristine and Z-type displaced QDs have been computed at the DFT level of theory using the Perdew, Burke, and Ernzerhof (PBE) exchange–correlation functional[49] using the CP2k 3.0 code[50]. All structures were fully relaxed in vacuum. Oscillator strengths were calculated from the matrix elements of the position operator. More in-depth details on the DFT simulations are in Supplementary Section 10.

Ultrafast pump–probe spectroscopy. Samples were pumped using 180 femtosecond pulses at 700 nm, created from the 1,028 nm fundamental (Pharos SP, 6W, Light Conversion) through nonlinear frequency mixing in an OPA (Orpheus, Light Conversion). Broadband probe pulses were generated in a sapphire crystal using the 1,028 nm fundamental. The pulses were delayed relative to the probe using a delay stage with maximum delay of 2.5 ns (Helios Spectrometer, Ultrafast Systems). Noise levels of 0.02 mOD (RMS) are achieved by integrating the measurements over 1 s (or 2,500 shots). The probe spectrum covers the visible–near-infrared window from 450 nm up to 1,620 nm. HgTe QDs were dispersed in a transparent solvent (tetrachloroethylene) to achieve optical densities of 0.1 at the first exciton transition typically. Samples were stirred during all measurements. No air-free sample handling was required as HgTe is, under our conditions, insensitive to oxidation, as is evidenced by a lack of PL peak shift or change in photoluminescent quantum yield when exposing samples to ambient conditions for several weeks. The average number of absorbed photons (or photo-generated excitons) at time zero $\langle N\rangle$ was calculated as:

$$\langle N\rangle = J_{\text{ph}}\sigma_{700}\frac{1-10^{-A_{0,700}}}{A_{0,700}}\log(e) \tag{3}$$

Here J_{ph} is the photon flux in photons cm^{-2} at 700 nm, σ_{700} is the absorption cross-section of the QDs at the pump wavelength of 700 nm and $A_{0,700}$ is the sample absorbance at 700 nm. The beam size used for calculating J_{ph} is measured using a Thorlabs CCD Camera Beam profiler. The additional factor corrects for variation of the pump fluence along the pump beam path length. The cross-section σ_{700} is determined starting from $\mu_{i,400}$ (see Supplementary Information) as[38]:

$$\sigma_{700} = V_{\text{QD}}\mu_{i,400}\frac{A_{0,700}}{A_{0,400}} \tag{4}$$

Here, V_{QD} is the volume of the quantum dot. Note that the (relative) error on V_{QD} is 32% due to the size distribution obtained through TEM analysis. This allows us to determine the scaling factor between pump fluence (mW) and absorbed photons for the TA experiments as $0.31 \pm 0.1\ \text{mW}^{-1}$. This translates into an error of 32% on all mentioned $\langle N\rangle$ values. We note that the calculation of $\langle N\rangle$ in thin films is very similar to the solution case, yet as the OD of the film at the pump wavelength is high (about 0.5) the correction factor becomes important.

Data availability. The authors declare that the main data supporting the findings of this study are available within the article and its Supplementary Information files. Extra data are available from the corresponding author upon request.

References

49. Perdew, J. P., Burke, K. & Ernzerhof, M. Generalized gradient approximation made simple. *Phys. Rev. Lett.* **77,** 3865–3868 (1996).
50. Iannuzzi, M., Schiffmann, F. & Vandevondele, J. CP2k: atomistic simulations of condensed matter systems. *Wiley Interdiscip. Rev. Comput. Mol. Sci.* **4,** 15–25 (2014).